

Behaviour of the Serre Equations in the Presence of Steep Gradients Revisited

J.P.A. Pitt^{a,*}, C. Zoppou^a, S.G. Roberts^a

^a*Mathematical Sciences Institute, Australian National University, Canberra, ACT 0200, Australia*

Abstract

We use various numerical methods to study the behaviour of the Serre equations in the presence of steep gradients, due to the lack of known analytical solutions for these problems. In keeping with the literature we study a class of initial condition problems that are a smooth approximation to the initial conditions of the dam-break problem. This class of initial condition problems allow us to observe the effect of varying steepness of the initial conditions on the solution of the Serre equations. To approximate the solution of the Serre equations we use numerical solutions from various methods. These numerical solutions are justified by demonstrating that as the resolution increases they converge to a numerical solution with little error in conservation, independent of the numerical method. We find four different structures of the converged numerical solutions depending on the steepness of the initial conditions. Two of these structures were observed in the literature, with the other two not being commonly found in the literature for these equations. The numerical solutions are then used to assess how well the analytical solution of the shallow water wave equations captures the mean behaviour of the solution of the Serre equations for the dam-break problem. Lastly the numerical solutions are used to evaluate the usefulness of asymptotic results in the literature to approximate the depth and location of the front of an undular bore.

Keywords: Serre equations, steep gradients, dam break

¹ 1. Introduction

² The behaviour of flows containing steep gradients are important to a range of prob-
³ lems in shallow water such as the propagation of a bore, the dam-break problem and
⁴ shoaling waves on a beach.

⁵ The Serre equations are used as a compromise between the non-dispersive shallow
⁶ water wave equations and the incompressible inviscid Euler equations for modelling
⁷ this behaviour. The Serre equations produce dispersive waves in the presence of steep

*Corresponding author

Email addresses: jordan.pitt@anu.edu.au (J.P.A. Pitt),
christopher.zoppou@anu.edu.au (C. Zoppou), stephen.roberts@anu.edu.au
(S.G. Roberts)

8 gradients as they do in the Euler equations [1]. However, unlike the Euler equations
9 there are efficient methods for solving the Serre equations [2–4], as there are for the
10 shallow water wave equations. The Serre equations are considered the most appro-
11 priate approximate model of dispersive waves up to the shore line [5, 6]. Therefore,
12 understanding the behaviour of the Serre equations in the presence of steep gradients
13 offers some insight into the behaviour of steep gradients for fluids more generally.

14 There are no known analytical solutions to problems containing steep gradients for
15 the Serre equations. To infer the structure of solutions to problems containing steep
16 gradients we have to resort to investigating numerical solutions of the Serre equations
17 for these problems.

18 Unfortunately, there are few examples in the literature which depict the behaviour
19 of numerical solutions to the Serre equations in the presence of steep gradients [1–
20 4, 7, 8]. These papers all present problems with discontinuous initial conditions [2–4]
21 or a smooth approximation to them [1, 7, 8]. Among these papers there are differences
22 in the structures of the numerical solutions, with some demonstrating undulations in
23 depth and velocity throughout the bore [3, 4, 7] and others showing a constant depth
24 and velocity state in the middle of the bore [1, 2, 8].

25 The mean behaviour of numerical solutions to the dam-break problem for the Serre
26 equations is consistent across the literature [1–4, 7, 8] and was demonstrated to be
27 well approximated by the analytical solution to the dam-break problem for the shallow
28 water wave equations [2, 8]. Expressions for the leading wave amplitude and speed of
29 an undular bore for the Serre equations were derived and verified for a range of undular
30 bores by El et al. [7]. These expressions were also shown to be valid for all the different
31 structures found in the literature [7, 8].

32 The first aim of this paper is to investigate and determine the cause of the different
33 behaviour that has been published in the literature for numerical solutions of the Serre
34 equations for problems containing steep gradients. We find that the undulations of a
35 bore can be damped to a constant depth and velocity state by the numerical diffusion
36 introduced by the method, as is the case for Le Métayer et al. [2]. Oscillation damping
37 can also occur due to the particular smoothing of the initial conditions, as is the case
38 for Mitsotakis et al. [1], El et al. [7] and Mitsotakis et al. [8]. We do find that over
39 long time periods the Serre equations damp these oscillations as they propagate, but
40 this natural decay is dominated by other factors in the literature.

41 The second aim of this paper is to assess the utility of the shallow water wave
42 equations and the results of El et al. [7] as guides for the evolution of an undular bore.
43 We find that for a range of dam-break problems the analytical solution of the shallow
44 water wave equations is a good approximation for the mean depth and velocity of the
45 Serre equations, extending the findings of Le Métayer et al. [2] and Mitsotakis et al.
46 [8] to a larger range of dam-break problems. It was also found that the results of El
47 et al. [7] are a good approximation to our numerical solutions and are only a slight
48 underestimation.

49 The first aim of this paper is achieved by demonstrating that our numerical solutions
50 are good approximations to the true solutions of the Serre equations. This is accom-
51 plished by demonstrating that as the resolution of a particular method is increased, the
52 numerical solutions converge to a numerical solution with little error in conservation,
53 and that this numerical solution is the same across the five different numerical meth-

ods. Three of the methods are the first, second and third-order methods presented by Zoppou et al. [4]. The first-order method is equivalent to the method of Le Métayer et al. [2]. The fourth method is a recreation of the second-order method used by El et al. [7]. Lastly, the fifth method is a second-order finite difference approximation to the Serre equations.

The second aim is accomplished by comparing our verified numerical solutions to the analytical solutions of the shallow water wave equations and the Whitham modulation results.

The paper is organised as follows, in Section 2 the Serre equations and the quantities they conserve are presented. In Section 3 the smoothed dam-break problem is defined, the measures of the relative difference between numerical solutions and the relative error in conservation are given. The analytical solution of the shallow water wave equations and the expressions for the amplitude and speed of the leading wave of an undular bore are given. In Section 4 the numerical methods and their important properties are presented. In Section 5 the four different structures in the solutions of smoothed dam-break problem for the Serre equations are determined using verified numerical solutions. The verified numerical solutions are also used to evaluate how well the analytical solution of the shallow water wave equations captures the mean behaviour of the solution of the Serre equations for the dam-break problem. The Whitham modulations results are also compared to the verified numerical solutions to test their veracity. Lastly, the Appendix presents the two finite difference methods in replicable detail.

2. Serre Equations

The Serre equations can be derived by integrating the full inviscid incompressible Euler equations over the water depth [9]. They can also be derived as an asymptotic expansion of the Euler equations [10]. Assuming a constant horizontal bed, the one-dimensional Serre equations are [11]

$$\frac{\partial h}{\partial t} + \frac{\partial(uh)}{\partial x} = 0 \quad (1a)$$

and

$$\underbrace{\frac{\partial(uh)}{\partial t} + \frac{\partial}{\partial x} \left(u^2 h + \frac{gh^2}{2} \right)}_{\text{Shallow Water Wave Equations}} + \underbrace{\frac{\partial}{\partial x} \left(\frac{h^3}{3} \left[\frac{\partial u}{\partial x} \frac{\partial u}{\partial x} - u \frac{\partial^2 u}{\partial x^2} - \frac{\partial^2 u}{\partial x \partial t} \right] \right)}_{\text{Dispersion Terms}} = 0. \quad (1b)$$

Serre Equations

Where $u(x, t)$ is the horizontal velocity over the depth of water $h(x, t)$, g is the acceleration due to gravity, x is the horizontal spatial variable and t is time.

The Serre equations are conservation laws for ‘mass’ (1a), ‘momentum’ (1b) and the Hamiltonian [12, 13]

$$\mathcal{H}(x, t) = \frac{1}{2} \left(hu^2 + \frac{h^3}{3} \left(\frac{\partial u}{\partial x} \right)^2 + gh^2 \right) \quad (2)$$

92 which is the total energy.

93 The total amount of a quantity q in a system in the spatial interval $[a, b]$ at a partic-
94 ular time t , is measured by

95
$$C_q(t) = \int_a^b q(x, t) dx.$$

96

97 Conservation of a quantity q implies that $C_q(0) = C_q(t)$ for all t provided the interval is
98 fixed and the system is closed. Our numerical methods should demonstrate conserva-
99 tion for the quantities h , uh and \mathcal{H} .

100 **3. Smoothed Dam Break Problem**

101 In this section we define a class of initial condition problems, called the smoothed
102 dam-break problem that we use throughout our numerical investigation. This class of
103 initial conditions are used in the literature [1, 8] to smoothly approximate the discon-
104 tinuous initial conditions of the dam-break problem. There is, no analytical solutions
105 of the Serre equations for the dam-break problem or an arbitrary smoothed dam-break
106 problem. Therefore, to demonstrate that our numerical solutions converge we use the
107 relative difference between numerical solutions. To demonstrate that our numerical
108 solutions have small errors in conservation we use the relative error in conservation.
109 Both of these measures are defined in this section.

110 The smoothed dam-break problem has the following initial conditions

111
$$h(x, 0) = h_0 + \frac{h_1 - h_0}{2} \left(1 + \tanh\left(\frac{x_0 - x}{\alpha}\right) \right) m, \quad (3a)$$

112

113 and

114
$$u(x, 0) = 0.0 \text{ m/s}. \quad (3b)$$

115

116 This represents a smooth transition centred around x_0 between a water depth of h_0
117 on the right and a water depth of h_1 on the left. Here α measures the distance over
118 which approximately 46% of that smooth transition between the two heights occurs.
119 Decreasing α increases the steepness of the initial conditions as can be seen in Figure
120 1 where $h_0 = 1m$ and $h_1 = 1.8m$. These are the same h_0 and h_1 values as those of the
121 smoothed dam-break problem of El et al. [7] and the dam-break problem of Le Métayer
122 et al. [2].

123 *3.1. Assessing validity of Numerical Solutions*

124 To demonstrate that our numerical solutions converge to a solution with little error
125 in conservation as the spatial resolution is increased we use two measures; the rela-
126 tive difference between numerical solutions of different resolutions and the error in
127 conservation. The relative difference between numerical solutions measures their con-
128 vergence, while the error in conservation measures how well the numerical solutions
129 conserve the quantities h , uh and \mathcal{H} .

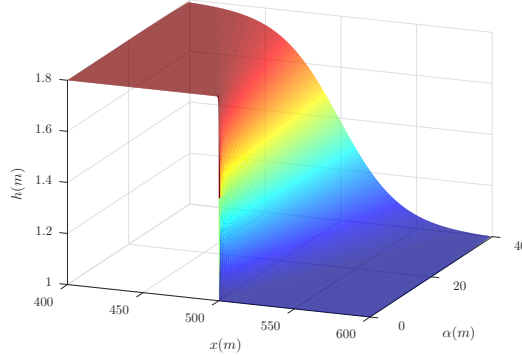


Figure 1: Initial conditions for smooth dam-break problems with $h_0 = 1m$, $h_1 = 1.8m$, $x_0 = 500m$ and various α .

130 We introduce the following notation for the spatial grids defined by x_i and the
 131 temporal grids defined by t^n upon which the numerical solutions are calculated. These
 132 grids are uniform so that $\Delta x = x_i - x_{i-1}$ for all i and $\Delta t = t^n - t^{n-1}$ for all n . We use
 133 subscripts and superscripts to denote where a quantity q is evaluated in the following
 134 way $q_i^n = q(x_i, t^n)$. Finally, the i th cell is the interval $[x_i - \Delta x/2, x_i + \Delta x/2]$ centred
 135 around x_i .

136 3.1.1. Convergence of Numerical Results

137 In these experiments, Δx was reduced by dividing it by 2 thus the finest grid with
 138 the smallest Δx contains all the locations x_i in any coarser grid. To measure the relative
 139 difference between quantities on these grids we compare them only on the coarser grid
 140 points x_i . For some quantity q we have our numerical approximation to it on the finest
 141 grid q^* and on the coarser grid q' , with the relative difference between the two being

$$142 \quad L_1^q = \frac{\sum_i |q'(x_i) - q^*(x_i)|}{\sum_i |q^*(x_i)|}. \quad (4)$$

144 3.1.2. Conserved Quantities

145 In the smoothed dam-break problem, the initial conditions (3) were integrated to get
 146 expressions for the total mass $C_h(0)$, the total momentum $C_{uh}(0)$ and the total Hamiltonian
 147 $C_{\mathcal{H}}(0)$. Provided x_0 is the midpoint of the spatial domain $[a, b]$ the totals for the
 148 conserved quantities are

$$149 \quad C_h(0) = \frac{h_1 + h_0}{2} (b - a),$$

$$152 \quad C_{uh}(0) = 0$$

154 and

$$155 \quad C_{\mathcal{H}}(0) = \frac{g}{4} \left(h_0^2 - h_1^2 + \alpha (h_1 - h_0)^2 \tanh \left(\frac{a - b}{2\alpha} \right) \right).$$

157
 158 To calculate how well we approximate the total amount of a quantity q in our nu-
 159 mercial solution we fit a quartic interpolant of the primitive variables h and u over a
 160 cell utilising neighbouring cells and then apply Gaussian quadrature with 3 points. The
 161 amount of q in each cell is summed across all cells to get the total amount of q in
 162 our numerical solution at time t , which we call $C_q^*(t)$. The error in conservation of a
 163 quantity q for a numerical solution is

164

$$C_1^q = \frac{|C_q(0) - C_q^*(t)|}{|C_q(0)|}. \quad (6)$$

165

166 Note that for uh the denominator is 0 and that there is a flux of momentum due to the
 167 unequal heights at both ends of the domain. To resolve these issues for uh the error in
 168 the conservation of uh is measured by

169

$$C_1^{uh} = \left| C_{uh}(0) - C_{uh}^*(t) - \frac{gt}{2} (h(b)^2 - h(a)^2) \right|. \quad (7)$$

170

171 3.2. Background for derived and observed comparisons

172 It was demonstrated by Le Métayer et al. [2] and Mitsotakis et al. [8] that the
 173 analytical solution of the shallow water wave equations for the dam-break problem
 174 captures the mean behaviour of the numerical solutions of the Serre equations to the
 175 dam-break problem [2] and the smoothed dam-break problem [8].

176 El et al. [7] derived an expression for the long term amplitude of the leading wave
 177 of an undular bore A^+ for the Serre equations. Since the front of an undular bore
 178 decomposes into solitons, the speed of the leading wave can be calculated from its
 179 amplitude.

180 To be self contained we present the analytical solution of the shallow water wave
 181 equations to the dam-break problem and the expressions derived by El et al. [7].

182 3.2.1. Shallow Water Wave Equation Analytical Solution

183 For the dam-break problem the shallow water wave equations, which are the Serre
 184 equations with dispersive terms neglected, can be solved analytically.

185 An example of the analytical solution of the shallow water wave equations for the
 186 dam-break problem is presented in Figure 2. Region I is the undisturbed water up-
 187 stream of the dam-break at constant height (h_1) and velocity (0m/s). Region II is the
 188 rarefaction fan connecting regions I and III. Regions III and IV are the constant height
 189 (h_2) and constant velocity (u_2) states which are separated by $x_{u_2} = x_0 + u_2 t$. Region V
 190 is the undisturbed water downstream at constant height (h_0) and velocity (0m/s) sep-
 191 arated from Region IV by a shock which travels at velocity S_2 . Expressions for the
 192 unknown quantities h_2 , u_2 and S_2 in terms of h_0 and h_1 were given by Wu et al. [14] as

193

$$h_2 = \frac{h_0}{2} \left(\sqrt{1 + 8 \left(\frac{2h_2}{h_2 - h_0} \frac{\sqrt{h_1} - \sqrt{h_2}}{\sqrt{h_0}} \right)^2} - 1 \right), \quad (8a)$$

194

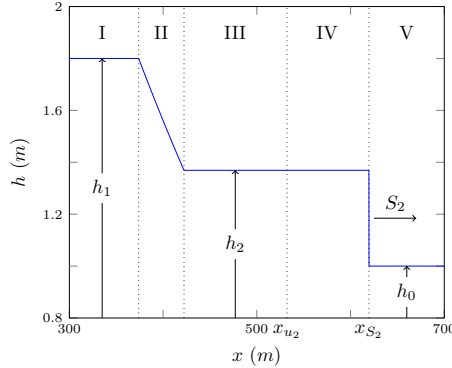


Figure 2: Analytical solution at $t = 30s$ of the dam-break problem for the shallow water wave equations with $h_0 = 1m$, $h_1 = 1.8m$ and $x_0 = 500m$.

195

196
197

$$u_2 = 2 \left(\sqrt{gh_1} - \sqrt{gh_2} \right) \quad (8b)$$

198 and

199
200

$$S_2 = \frac{h_2 u_2}{h_2 - h_0}. \quad (8c)$$

201 Applying (8) to our dam-break heights of interest; $h_0 = 1m$ and $h_1 = 1.8m$ results
202 in $h_2 = 1.36898m$, $u_2 = 1.074975 m/s$ and $S_2 = 3.98835 m/s$ which are shown in
203 Figure 2 for $t = 30s$. The location of the front of the bore for the shallow water wave
204 equations at time t is thus $x_{S_2}(t) = x_0 + S_2 t$.

205 *3.2.2. Whitham Modulation for Undular Bores of the Serre Equations*

206 Utilizing Whitham modulation theory for a one-phase periodic travelling wave an
207 asymptotic analytical expression for the amplitude A^+ and speed S^+ of the leading
208 wave was derived by El et al. [7]. An example of an undular bore is shown in Figure 3.
209 The derived expressions for A^+ and S^+ are

$$210 \quad \frac{\Delta}{(A^+ + 1)^{1/4}} - \left(\frac{3}{4 - \sqrt{A^+ + 1}} \right)^{21/10} \left(\frac{2}{1 + \sqrt{A^+ + 1}} \right)^{2/5} = 0 \quad (9a)$$

212 and

213

$$S^+ = \sqrt{g(A^+ + 1)} \quad (9b)$$

where $\Delta = h_b/h_0$, and h_b is the height of the bore. The height of the bore created by
the dam-break problem in (9a) used by El et al. [7] was

$$h_b = \frac{1}{4} \left(\sqrt{\frac{h_1}{h_0}} + 1 \right)^2.$$

215 For our dam-break heights of interest $h_0 = 1m$ and $h_1 = 1.8m$ we obtain $h_b = 1.37082m$,
216 $\Delta = 1.37082$, $A^+ = 1.73998m$ and $S^+ = 4.13148m/s$. The location of
217 the leading wave of an undular bore at time t is then $x_{S^+}(t) = x_0 + S^+ t$.

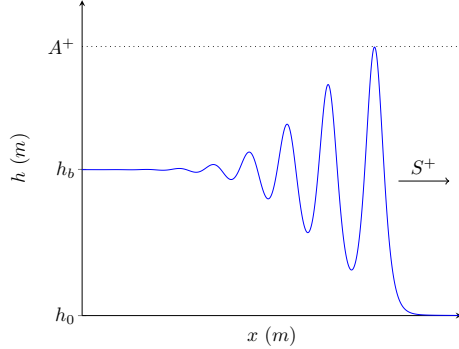


Figure 3: Demonstration of quantities obtained by Whitham modulation for undular bores of the Serre equations.

218 4. Numerical Methods

219 Five numerical schemes are used to investigate the behaviour of the Serre equations
 220 in the presence of steep gradients. The first (\mathcal{V}_1), second (\mathcal{V}_2) and third-order (\mathcal{V}_3)
 221 finite difference finite volume methods of Zoppou et al. [4]. The second-order finite
 222 difference method of El et al. [7] (\mathcal{E}) and a second-order finite difference method (\mathcal{D})
 223 that can be found in the Appendix.

224 The \mathcal{V}_i methods are stable under a Courant-Friedrichs-Lowy (CFL) condition
 225 such as the one presented by A. Harten [15]. The \mathcal{V}_i methods have demonstrated
 226 the appropriate order of convergence for smooth problems [4]. Furthermore, \mathcal{V}_2 and
 227 \mathcal{V}_3 have been validated against experimental data containing steep gradients [4]. The
 228 two methods \mathcal{D} and \mathcal{E} were found to be stable under the CFL condition as well.

229 Generally, we found that \mathcal{V}_1 is the worst performing method due to its numeri-
 230 cal diffusion [4]. Of the high-order methods \mathcal{E} is the worst performing, introducing
 231 dispersive errors.

232 5. Numerical Results

233 We investigate the behaviour of the Serre equations in the presence of steep gradi-
 234 ents by numerically solving the smoothed dam-break problem while varying the steep-
 235 ness of the initial conditions. As $\Delta x \rightarrow 0$ our numerical solutions should better ap-
 236 proximate the true solution of the Serre equations. If our numerical solutions to a
 237 smoothed dam-break problem converge to the same numerical solution with little error
 238 in conservation as $\Delta x \rightarrow 0$ for each method, then this numerical solution is considered
 239 an accurate approximate solution to that smoothed dam-break problem for the Serre
 240 equations.

241 This process validates our numerical solutions for the smoothed dam-break prob-
 242 lem, and thus validates our numerical methods to approximate the solution of the Serre
 243 equations in the presence of steep gradients. With a validated model we can compare
 244 the numerical solution to the analytical solution of the shallow water wave equations
 245 for the dam-break problem and the results of El et al. [7].

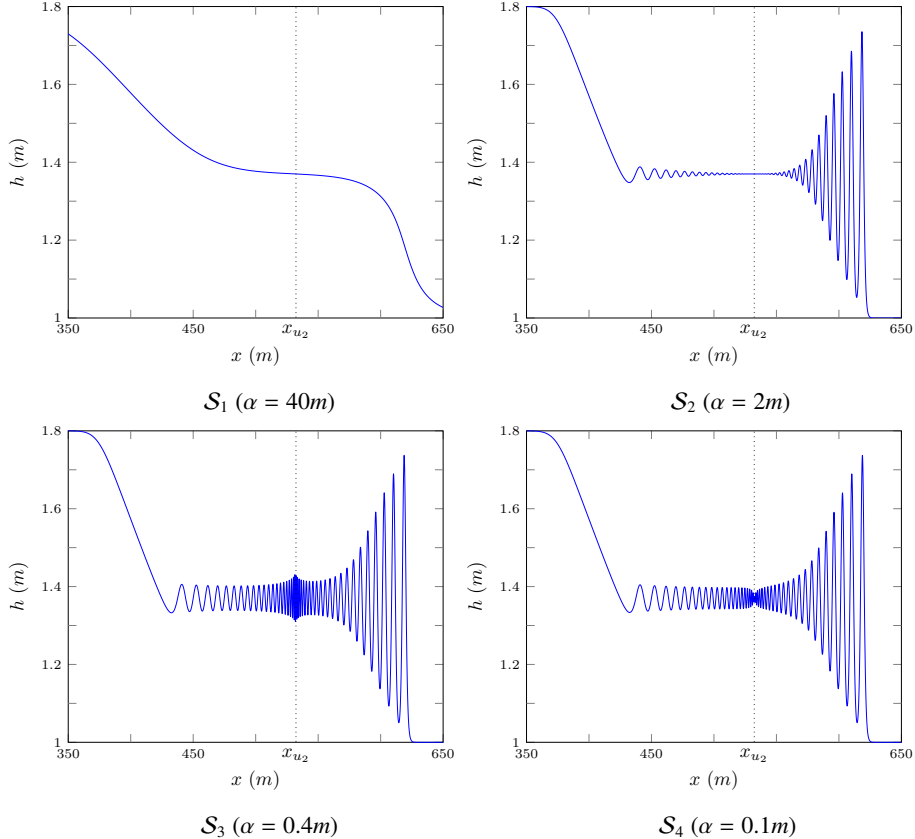


Figure 4: Numerical results of \mathcal{V}_3 with $\Delta x = 10/2^{11}m$ (—) at $t = 30s$ for various smooth dam-break problems demonstrating the different observed structures.

Throughout most of this section we are interested in the numerical solution at $t = 30s$ to the smoothed dam-break problem with $h_0 = 1m$, $h_1 = 1.8m$ and $x_0 = 500m$ while allowing for different α values. All numerical methods used $\Delta t = 0.01\Delta x$ which is smaller than required by the CFL condition, ensuring stability of our schemes. The method \mathcal{V}_2 requires an input parameter to its slope limiter and this was chosen to be $\theta = 1.2$ [4]. The spatial domain was $[0m, 1000m]$ with the following Dirichlet boundary conditions, $u = 0m/s$ at both boundaries, $h = 1.8m$ on the left and $h = 1m$ on the right.

5.1. Observed Structures of the Numerical Solutions

We observe that there are four different structures for the converged to numerical solution depending on the chosen α . They are the ‘non-oscillatory’ structure \mathcal{S}_1 , the ‘flat’ structure \mathcal{S}_2 , the ‘node’ structure \mathcal{S}_3 and the ‘growth’ structure \mathcal{S}_4 . An example of each of these structures is shown in Figure 4 which were obtained using \mathcal{V}_3 with $\Delta x = 10/2^{11}m$.

The four structures are identified by the dominant features of the numerical solutions in regions III and IV. They correspond to different structures in the numerical

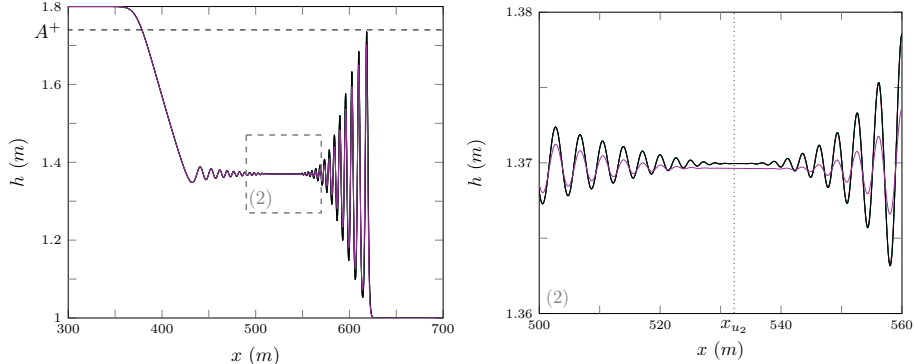


Figure 5: Numerical solutions of \mathcal{D} (blue), \mathcal{E} (red), \mathcal{V}_3 (green), \mathcal{V}_2 (black) and \mathcal{V}_1 (purple) with $\Delta x = 10/2^{11}m$ at $t = 30s$ for the smooth dam-break problem with $\alpha = 2m$.

solutions that have been presented in the literature. From Figure 4 it can be seen that as α is decreased, steepening the initial conditions, the numerical solutions demonstrate an increase in the size and number of oscillations particularly around x_{u_2} . We observe that the difference between \mathcal{S}_2 , \mathcal{S}_3 and \mathcal{S}_4 is the amplitude of the oscillations in regions III and IV.

For the non-oscillatory and flat structures there is excellent agreement between all higher-order numerical methods at our highest resolution $\Delta x = 10/2^{11}m$. An illustration of this agreement is given in Figure 5 for \mathcal{S}_2 which is the most difficult to resolve of the two structures. However, the first-order method \mathcal{V}_1 suppresses oscillations present in the numerical solutions of other methods due to its diffusive errors [4], requiring lower Δx to resolve them.

5.1.1. Non-oscillatory Structure

The \mathcal{S}_1 structure is the result of a large α , which causes the front of this flow to not be steep enough to generate undulations over short time periods. As the system evolves the front will steepen due to non-linearity and undulations will develop.

The structure \mathcal{S}_1 is not present in the literature as no authors chose large enough α , as such a large α poorly approximates the dam-break problem. An example of this structure can be seen in Figure 6 for $\alpha = 40m$ using \mathcal{V}_3 with various Δx values. Because this is not a very steep problem all numerical results are visually identical for all $\Delta x < 10/2^4m$.

From Table 1 it can be seen that not only have these solutions converged visually but the L_1 measures demonstrate that we have reached convergence to round-off error by $\Delta x = 10/2^8m$ after which the relative difference between numerical solutions plateau.

Table 1 also demonstrates that the error in conservation of the numerical solutions are at round-off error for h and \mathcal{H} . The conservation of uh is poor because the smoothed dam-break has such a large α that $h(0m) \neq 1.8m$ and $h(1000m) \neq 1m$, causing unequal fluxes in momentum at the boundaries.

As stated above when $\Delta x = 10/2^{11}m$ the numerical solutions from all methods are visually identical for this smoothed dam-break problem.

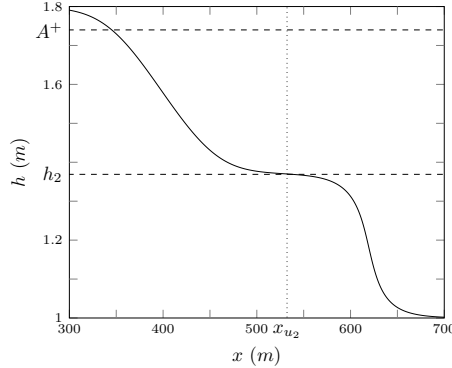


Figure 6: Numerical solutions of \mathcal{V}_3 at $t = 30s$ for smooth dam-break problem with $\alpha = 40m$ for $\Delta x = 10/2^{10}m$ (—), $10/2^8m$ (—), $10/2^6m$ (—) and $10/2^4m$ (—).

The convergence of the numerical solutions as $\Delta x \rightarrow 0$ to a numerical solution with small error in conservation, independent of the method demonstrates that we have accurately solved the smoothed dam-break problem with $\alpha = 40m$. Therefore, the S_1 structure should be observed in the solutions of the Serre equations for the smoothed dam-break problem for sufficiently large α .

5.1.2. Flat Structure

The most common structure observed in the literature [1, 2, 8] is the Flat structure, S_2 . It is observed when the initial conditions are steep enough such that the bore that develops has undulations. This structure consists of oscillations in regions III and IV which are separated by a constant height state around x_{u_2} . An example of the S_2 structure can be seen in the numerical solutions presented in Figure 7 where $\alpha = 2m$.

As Δx decreases the numerical solutions converge so that by $\Delta x = 10/2^8m$ the solutions for higher Δx are visually identical. Table 1 demonstrates that although we have convergence visually, the L_1 measures are still decreasing and are larger than round-off error. Likewise the C_1 measures are still decreasing and have only reached round-off error for h . This indicates that to attain full convergence of the numerical solutions of this smoothed dam-break problem down to round-off error using \mathcal{V}_3 would require an even smaller Δx . The relative difference between numerical solutions is small and the numerical solutions exhibit good conservation. Therefore, our highest resolution numerical solution is a good approximation to any numerical solutions with lower Δx values. Furthermore, Figure 5 demonstrates that the highest resolution numerical solution of all higher-order methods are the same.

Using \mathcal{V}_3 with $\Delta x = 10/2^{11}m$ we have not attained the desired full convergence of the numerical solutions to one with little conservation error, independent of the particular method. However, we have demonstrated that we have obtained a very good approximation to such a numerical solution. Therefore, our highest resolution numerical solution is an accurate approximate solution of the Serre equations for the smoothed dam-break problem with $\alpha = 2m$. Implying that the S_2 structure should be observed in solutions of the Serre equations for smooth dam-break problems with similar α values.

α	Δx	C_1^h	C_1^{uh}	C_1^H	L_1^h	L_1^u
40	$10/2^4$	$2.00 \cdot 10^{-11}$	$1.77 \cdot 10^{-6}$	$1.23 \cdot 10^{-8}$	$1.74 \cdot 10^{-7}$	$2.90 \cdot 10^{-6}$
40	$10/2^6$	$1.07 \cdot 10^{-11}$	$1.50 \cdot 10^{-6}$	$1.49 \cdot 10^{-10}$	$2.57 \cdot 10^{-9}$	$4.19 \cdot 10^{-8}$
40	$10/2^8$	$8.77 \cdot 10^{-13}$	$5.49 \cdot 10^{-7}$	$3.77 \cdot 10^{-13}$	$6.08 \cdot 10^{-11}$	$5.28 \cdot 10^{-10}$
40	$10/2^{10}$	$1.77 \cdot 10^{-11}$	$2.21 \cdot 10^{-8}$	$3.56 \cdot 10^{-11}$	$2.54 \cdot 10^{-11}$	$6.49 \cdot 10^{-11}$
<hr/>						
2	$10/2^4$	$4.90 \cdot 10^{-14}$	$5.10 \cdot 10^{-3}$	$8.69 \cdot 10^{-4}$	$5.02 \cdot 10^{-3}$	$6.77 \cdot 10^{-2}$
2	$10/2^6$	$2.51 \cdot 10^{-13}$	$2.18 \cdot 10^{-4}$	$6.58 \cdot 10^{-5}$	$4.14 \cdot 10^{-4}$	$5.20 \cdot 10^{-3}$
2	$10/2^8$	$9.81 \cdot 10^{-13}$	$7.72 \cdot 10^{-7}$	$5.01 \cdot 10^{-7}$	$6.00 \cdot 10^{-6}$	$7.59 \cdot 10^{-5}$
2	$10/2^{10}$	$3.95 \cdot 10^{-12}$	$5.56 \cdot 10^{-9}$	$6.13 \cdot 10^{-9}$	$1.76 \cdot 10^{-7}$	$2.33 \cdot 10^{-6}$
<hr/>						
0.4	$10/2^4$	$9.00 \cdot 10^{-14}$	$4.82 \cdot 10^{-3}$	$1.02 \cdot 10^{-3}$	$6.79 \cdot 10^{-3} \dagger$	$9.93 \cdot 10^{-2} \dagger$
0.4	$10/2^6$	$2.40 \cdot 10^{-13}$	$2.41 \cdot 10^{-4}$	$1.11 \cdot 10^{-4}$	$8.89 \cdot 10^{-4} \dagger$	$1.13 \cdot 10^{-2} \dagger$
0.4	$10/2^8$	$9.68 \cdot 10^{-13}$	$7.57 \cdot 10^{-7}$	$2.25 \cdot 10^{-6}$	$1.53 \cdot 10^{-5} \dagger$	$1.91 \cdot 10^{-4} \dagger$
0.4	$10/2^{10}$	$3.91 \cdot 10^{-12}$	$4.95 \cdot 10^{-9}$	$2.01 \cdot 10^{-8}$	$3.61 \cdot 10^{-7} \dagger$	$5.00 \cdot 10^{-6} \dagger$
<hr/>						
0.1	$10/2^4$	$7.60 \cdot 10^{-14}$	$4.82 \cdot 10^{-3}$	$1.06 \cdot 10^{-3}$	$7.04 \cdot 10^{-3} \dagger$	$1.02 \cdot 10^{-1} \dagger$
0.1	$10/2^6$	$2.40 \cdot 10^{-13}$	$2.39 \cdot 10^{-4}$	$1.44 \cdot 10^{-4}$	$1.02 \cdot 10^{-3} \dagger$	$1.28 \cdot 10^{-2} \dagger$
0.1	$10/2^8$	$9.79 \cdot 10^{-13}$	$2.21 \cdot 10^{-7}$	$1.20 \cdot 10^{-5}$	$2.86 \cdot 10^{-5} \dagger$	$3.46 \cdot 10^{-4} \dagger$
0.1	$10/2^{10}$	$3.92 \cdot 10^{-12}$	$4.46 \cdot 10^{-8}$	$7.61 \cdot 10^{-7}$	$4.99 \cdot 10^{-7} \dagger$	$6.40 \cdot 10^{-6} \dagger$

Table 1: All errors in conservation C_1^q for the conserved quantities and relative differences L_1^q of the primitive variables for numerical solutions of \mathcal{V}_3 . L_1^q uses the numerical solution with $\Delta x = 10/2^{11}m$ as the high resolution basis of comparison and \dagger indicates the omission of the interval $[520m, 540m]$ from the comparison.

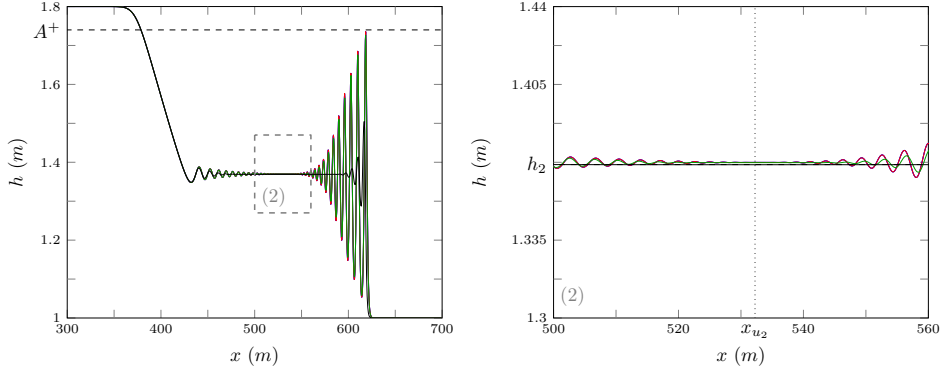


Figure 7: Numerical solutions of \mathcal{V}_3 at $t = 30s$ for the smooth dam-break problem with $\alpha = 2m$ for $\Delta x = 10/2^{10}m$ (blue), $10/2^8m$ (red), $10/2^6m$ (green) and $10/2^4m$ (black).

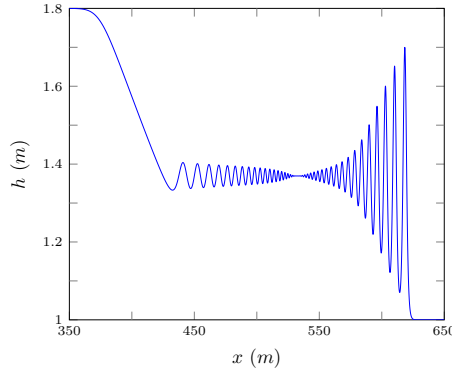


Figure 8: Numerical solution of \mathcal{V}_1 at $t = 30s$ for the smooth dam-break problem with $\alpha = 0.001m$ for $\Delta x = 10/2^{11}m$ (blue).

These numerical solutions compare well with those of Mitsotakis et al. [8] who use the same α but different h_0 and h_1 values and observe the \mathcal{S}_2 structure. We found that we observed this structure for all numerical method's numerical solutions to the smoothed dam-break problem with α values as low as $1m$ and $\Delta x = 10/2^{11}m$. The numerical solutions of Mitsotakis et al. [1] use $\alpha = 1m$ but different heights and observe the structure \mathcal{S}_2 . Therefore Mitsotakis et al. [8] and Mitsotakis et al. [1] observe the \mathcal{S}_2 structure in their numerical results due to their choice of α for the smoothed dam-break problem.

The first-order method \mathcal{V}_1 is diffusive [4] and damps oscillations that are present in the numerical solutions of higher-order methods as in Figure 5. We find that for any smoothed dam-break problem with $\alpha \leq 4m$ and the dam-break problem our numerical solutions with \mathcal{V}_1 at $t = 30s$ using $\Delta x = 10/2^{11}m$ only observe the \mathcal{S}_2 structure. This is evident in Figure 8 with the numerical solutions of \mathcal{V}_1 using our finest grid where $\Delta x = 10/2^{11}m$ for our steepest initial conditions where $\alpha = 0.001m$. Therefore, Le Métayer et al. [2] using the diffusive \mathcal{V}_1 with their chosen Δx and Δt , which are larger than our Δx and Δt could only observe the \mathcal{S}_2 structure.

335 *5.1.3. Node Structure*

336 The node structure, \mathcal{S}_3 was observed by El et al. [7]. The \mathcal{S}_3 structure has oscillations throughout regions III and IV that decay to a node at x_{u_2} as can be seen in Figure 9 where $\alpha = 0.4m$.

339 Figure 9 demonstrates that our numerical solutions have not converged, however
340 this is only in the area around x_{u_2} . Due to the large difference in numerical solutions
341 around x_{u_2} the L_1 measure over the area around x_{u_2} would not be insightful. However,
342 by omitting this region we can gain some knowledge about how well our solutions
343 agree away from x_{u_2} . This was performed for the relevant L_1 measures in Table 1
344 by omitting the interval $[520m, 540m]$. These modified L_1 measures demonstrate that
345 while our numerical results have visually converged outside this interval, they have not
346 converged down to round-off error.

347 Table 1 demonstrates that the C_1 measures are still decreasing and have only attained
348 round-off error for h . Therefore, to resolve the desired convergence of the numerical
349 solutions to one with small error in conservation using \mathcal{V}_3 would require even
350 smaller Δx values.

351 There is good agreement across different numerical methods for $\Delta x = 10/2^{11}m$ as
352 can be seen in Figure 10. In particular all the higher-order methods exhibit the same
353 structure and only disagree in a very small region around x_{u_2} . We observe that the
354 numerical solutions of the worst higher-order method \mathcal{E} has not converged well to the
355 numerical solutions of the other higher-order methods.

356 We have only obtained a good approximation to the desired numerical solution as
357 $\Delta x \rightarrow 0$ away from x_{u_2} . However, our highest resolution numerical solutions from
358 various higher-order methods are very similar. This suggests that again although we
359 do not have full convergence, our highest resolution numerical solution is a good ap-
360 proximation to the desired numerical solution over the whole domain. Therefore, our
361 highest resolution numerical solutions are an accurate representation of the solutions of
362 the Serre equations for this smoothed dam-break problem. Therefore, the \mathcal{S}_3 structure
363 should be observed in the solutions of the Serre equations for the smoothed dam-break
364 problem with $\alpha = 0.4m$.

365 These numerical solutions support the findings of El et al. [7] who also use some
366 smoothing [16] but do not report what smoothing was performed. Using their method
367 \mathcal{E} and similar Δx to El et al. [7] we observe the \mathcal{S}_4 “growth structure” in the numerical
368 solution for α values smaller than $0.1m$, indicating that the smoothing performed by El
369 et al. [7] limited their observed behaviour to just the \mathcal{S}_3 structure.

370 *5.1.4. Growth Structure*

371 The \mathcal{S}_4 “growth structure”, which has hitherto not been commonly published in
372 the literature features a growth in the oscillation amplitude around x_{u_2} . An example
373 of the growth structure can be seen for \mathcal{V}_3 ’s numerical solutions in Figure 11 to the
374 smoothed dam-break problem with $\alpha = 0.1m$. This structure was observed in the
375 numerical solutions of \mathcal{V}_3 for $\Delta x = 10/2^{11}m$ at $t = 30s$ for α values as low as $0.001m$
376 and even for the dam-break problem.

377 Figure 11 shows that this structure can only be observed for $\Delta x = 10/2^{10}m$, with
378 poor convergence of the numerical results around x_{u_2} . Again our L_1 measures in Table
379 1 omit the interval $[520m, 540m]$ in the numerical solutions. This demonstrates that

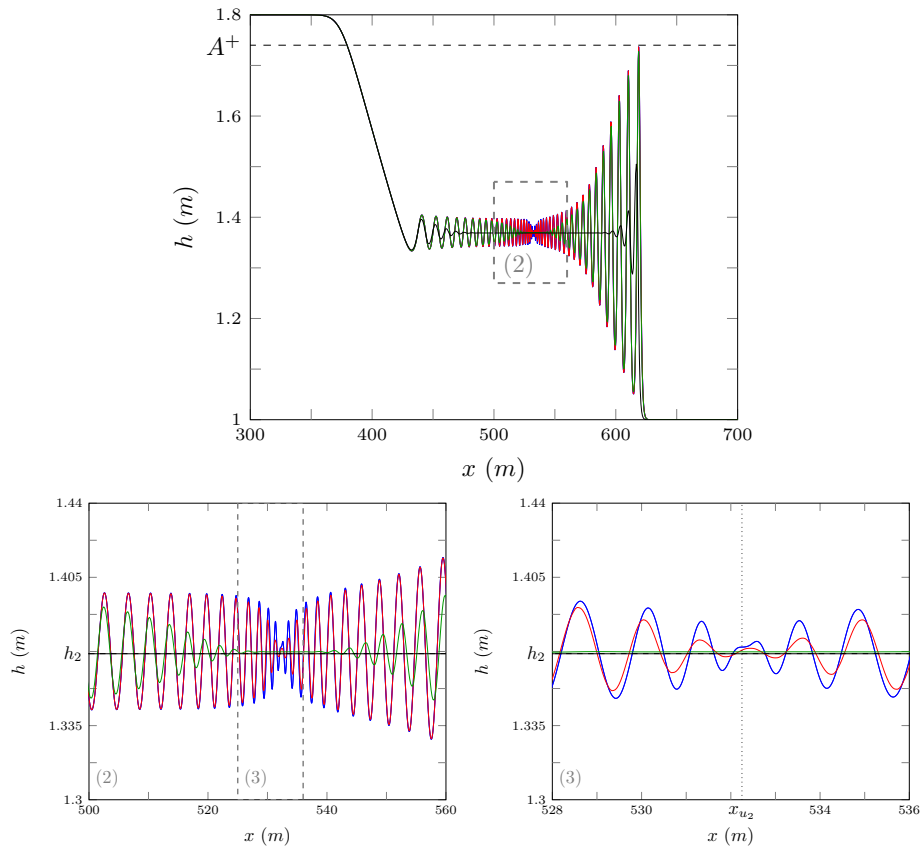


Figure 9: Numerical solutions of V_3 at $t = 30s$ for the smooth dam-break problem with $\alpha = 0.4m$ for $\Delta x = 10/2^{10}m$ (blue), $10/2^8m$ (red), $10/2^6m$ (green) and $10/2^4m$ (black).

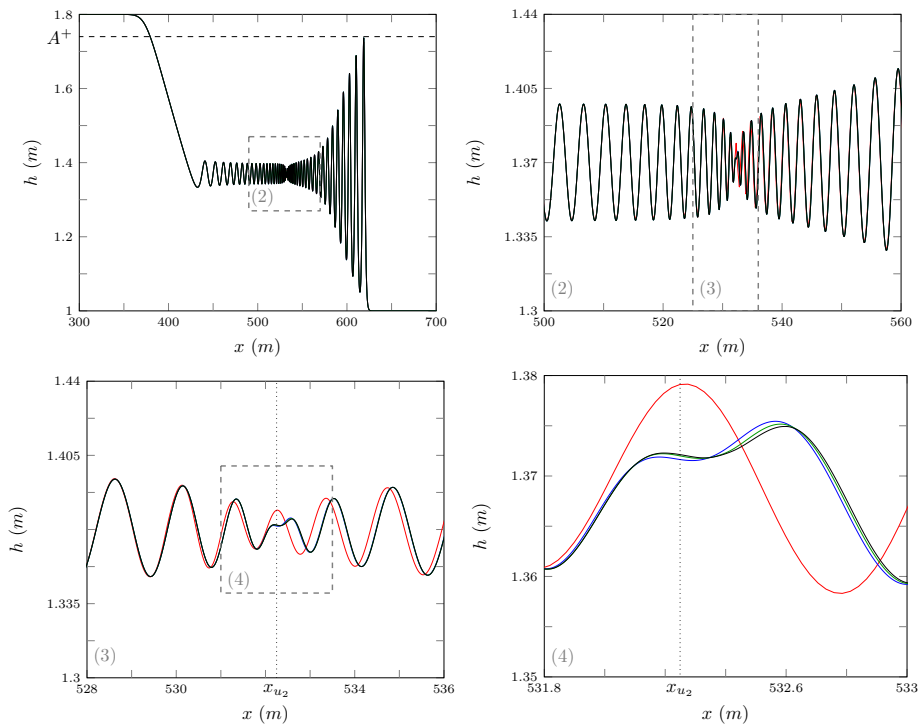


Figure 10: Numerical solutions of \mathcal{D} (—), \mathcal{E} (—), \mathcal{V}_3 (—) and \mathcal{V}_2 (—) at $t = 30s$ with $\Delta x = 10/2^{11}m$ for the smoothed dam-break problem with $\alpha = 0.4m$.

380 although we have visual convergence away from x_{u_2} our numerical solutions have not
381 converged to round-off error as $\Delta x \rightarrow 0$. The C_1 measures in Table 1 are still decreasing
382 and have only attained round-off error for h , although for uh and \mathcal{H} the errors in
383 conservation are small. These measures continue the trend in Table 1 where smaller
384 α 's and thus steeper initial conditions lead to larger L_1 and C_1 measures because these
385 problems are more difficult to solve accurately.

386 Figure 12 demonstrates that our numerical solutions for $\Delta x = 10/2^{11}m$ with the
387 best methods \mathcal{D} , \mathcal{V}_3 and \mathcal{V}_2 disagree for only a few oscillations around x_{u_2} . Since both
388 \mathcal{D} and \mathcal{E} are second-order finite difference methods their errors are dispersive. These
389 dispersive errors manifest in the numerical solutions of both methods as an increase
390 in the amplitude of oscillations particularly around x_{u_2} . Because the dispersive errors
391 of \mathcal{E} are larger than \mathcal{D} more oscillations are observed. The \mathcal{V}_3 method was shown to
392 be diffusive by Zoppou et al. [4] and therefore its numerical solutions underestimate
393 the size and number of oscillations. Therefore, the true solution of the Serre equations
394 should be between the dispersive method \mathcal{D} and the diffusive method \mathcal{V}_3 , and thus will
395 possess the \mathcal{S}_4 structure.

396 The numerical solutions of \mathcal{D} and \mathcal{V}_3 acting as upper and lower bounds respectively
397 for the oscillation amplitude as Δx is reduced is demonstrated in Figure 13 using
398 the maximum of h in the interval $[520m, 540m]$. From this figure it is clear that the
399 amplitudes of the numerical solutions of \mathcal{D} converge down to the limit as the resolution
400 is increased while the numerical solution amplitudes of \mathcal{V}_3 converge up to it. This
401 shows that we have effectively bounded the true solution of the Serre equations. Un-
402 fortunately, \mathcal{V}_3 could not be run in reasonable computational times with lower Δx , but
403 the numerical solutions of \mathcal{D} show that doing so is unnecessary.

404 These results indicate that the solutions of the Serre equations to the smoothed
405 dam-break problem with sufficiently small α values should exhibit a growth structure at
406 $t = 30s$, even though we have not precisely resolved all the oscillations in our numerical
407 solutions.

408 It was found that decreasing α did increase the amplitude of the oscillations around
409 x_{u_2} but not drastically. For \mathcal{V}_3 with $\Delta x = 10/2^{11}m$ and $\alpha = 0.001m$ the oscillations in
410 h were bounded by the interval $[1.28m, 1.46m]$. Of particular note is that the number of
411 oscillations are the same in Figures 10 and 12 for the best methods even though they
412 have different structures.

413 By changing the interval and desired time for the numerical solution, Δx could be
414 lowered further so that by $t = 3s$ our numerical solutions have reached full convergence
415 for α values as low as $0.001m$. This allows us to show that the height of the oscillations
416 for the solution of the Serre equation to the smoothed dam-break problem are bounded
417 at $t = 3s$ as $\alpha \rightarrow 0$. Figure 14 demonstrates this for the numerical solutions of \mathcal{V}_3 with
418 $\Delta x = 10/2^{13}m$.

419 5.2. Shallow water wave equation comparison

420 The analytical solutions of shallow water wave equations have been used as a guide
421 for the mean behaviour of the solution of the Serre equations for the dam-break problem
422 in the literature [2, 8].

423 To assess the applicability of this the mean bore depth and mean fluid velocity in
424 the interval $[x_{u_2} - 50m, x_{u_2} + 50m]$ were calculated from our numerical solution to the

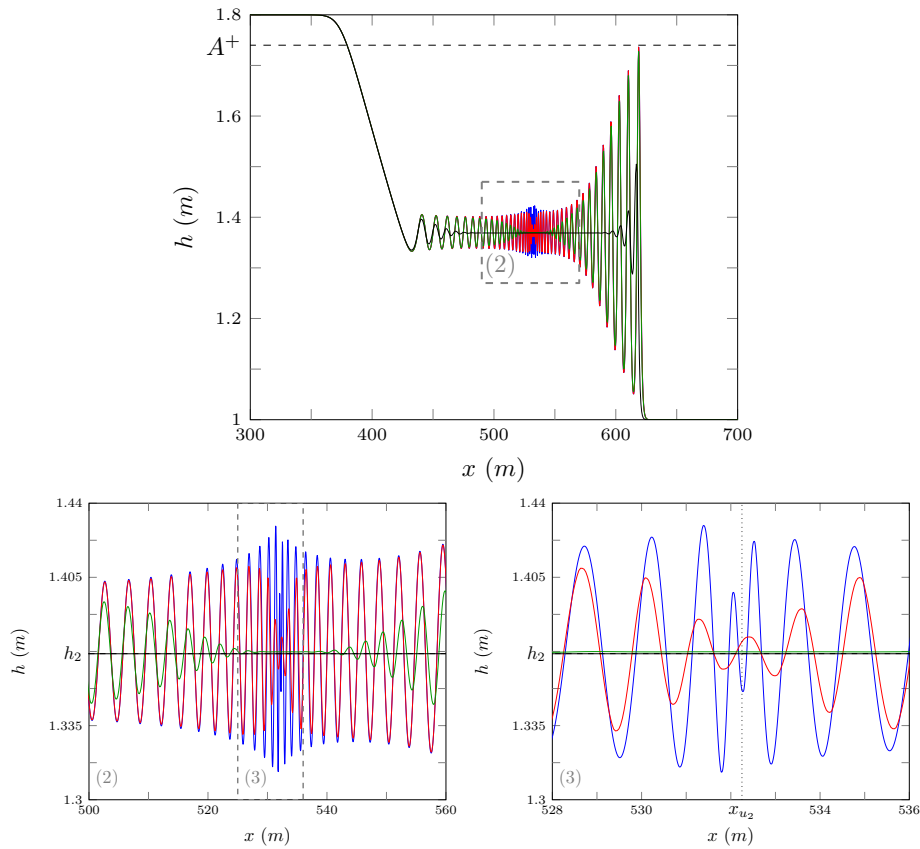


Figure 11: Numerical solutions of \mathcal{V}_3 at $t = 30s$ for the smooth dam-break problem with $\alpha = 0.1m$ for $\Delta x = 10/2^{10}m$ (blue), $10/2^8m$ (red), $10/2^6m$ (green) and $10/2^4m$ (black).

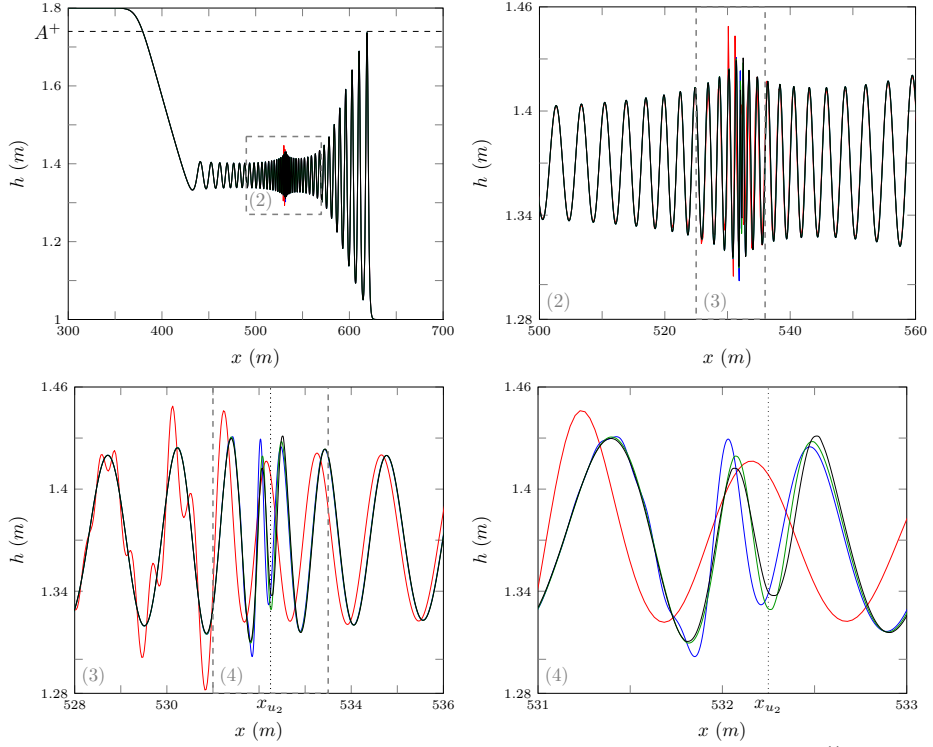


Figure 12: Numerical solutions of \mathcal{D} (blue line), \mathcal{E} (red line), \mathcal{V}_3 (green line) and \mathcal{V}_2 (black line) at $t = 30s$ with $\Delta x = 10/2^{11}m$ for the smoothed dam-break problem with $\alpha = 0.1m$.

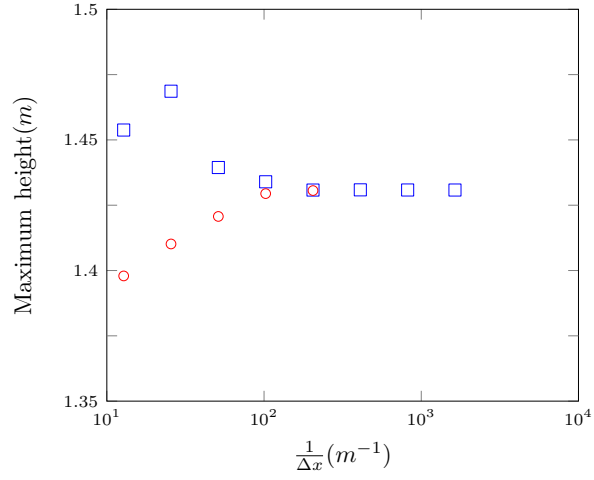


Figure 13: Maximum height of numerical solution of the smoothed dam-break problem with $\alpha = 0.4m$ at $t = 30s$ inside the interval [520m, 540m] using \mathcal{D} (blue square) and \mathcal{V}_3 (red circle).

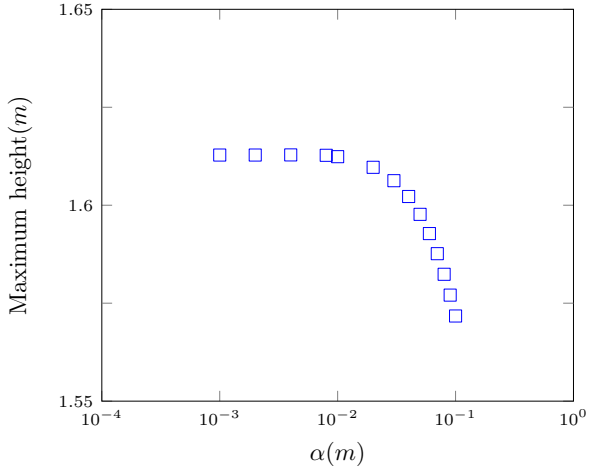


Figure 14: Maximum height of numerical solution around x_{u_2} at $t = 3s$ of various smoothed dam-break problem as α decreases, using \mathcal{V}_3 (□) with $\Delta x = 10/2^{13}m$.

425 smoothed dam-break problem with various height ratios. These means were compared
 426 to their approximations from the analytic solution of the dam-break problem for the
 427 shallow water wave equations h_2 and u_2 . The results of this can be seen in Figure 15
 428 for numerical solutions of \mathcal{V}_3 with $\Delta x = 10/2^9m$ to the smoothed dam-break problem
 429 at $t = 100s$ with $\alpha = 0.1m$ where h_0 is fixed and h_1 is varied.

430 We use a final time of $t = 100s$ as it allows the internal structure of the bore to
 431 develop more fully giving a more reliable mean estimate, as a consequence we resort
 432 to a coarser grid to keep the run-times reasonable. We find that decreasing Δx does
 433 not significantly alter the mean of u and h . We also find that increasing α also does
 434 not significantly alter the mean of h and u . Therefore, the mean behaviour of the
 435 converged conservative solution and thus the mean behaviour of the true solution of
 436 the Serre equations to the dam-break problem is captured by this numerical solution.

437 It can be seen that h_2 and u_2 are good approximations to the mean behaviour of
 438 the fluid inside the bore for a range of different aspect ratios. Although, as h_1/h_0
 439 increases this approximation becomes worse, so that h_2 becomes an underestimate and
 440 u_2 becomes an overestimate.

441 We find that for $h_1/h_0 = 1.8$ the mean values of h and u inside the bore for the Serre
 442 equations are not equal to h_2 and u_2 . This can be seen in Figure 16 for the numerical
 443 solutions of \mathcal{V}_3 with $\Delta x = 10/2^9m$ to the smoothed dam-break problem with $\alpha = 0.1m$
 444 at $t = 300s$. It can be seen that u_2 is an overestimate of u and h_2 is an underestimate
 445 of h , although the difference between these values and the mean behaviour of the Serre
 446 equations is small and only noticeable over long time periods.

447 The location of the leading wave of the Serre equations is poorly approximated
 448 by the location of the front of a bore in the shallow water wave equations. This is
 449 evident in \mathcal{V}_3 's numerical solution to the smoothed dam-break problem with $\alpha = 0.1m$
 450 at $t = 300s$ using $\Delta x = 10/2^9m$, which is shown in Figure 17.

451 We note that the S_4 structure present in the numerical solutions using this method

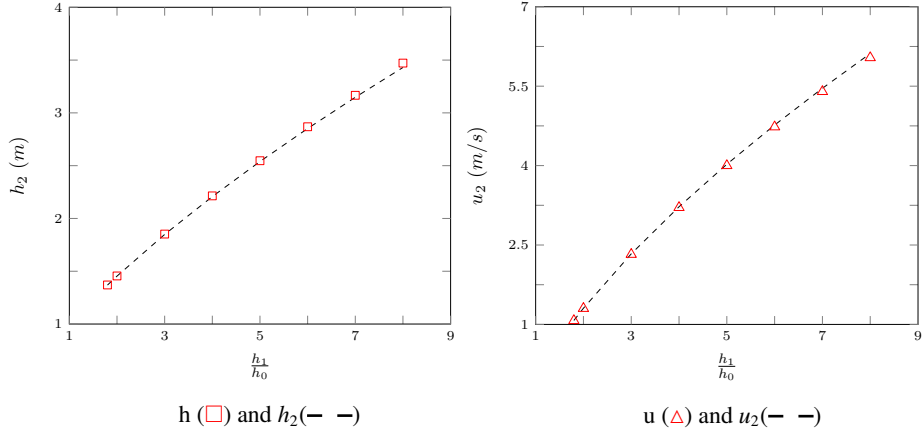


Figure 15: Comparison between mean behaviour inside the bore of the Serre equations and the analytic solution of the shallow water wave equations for a range of different aspect ratios.

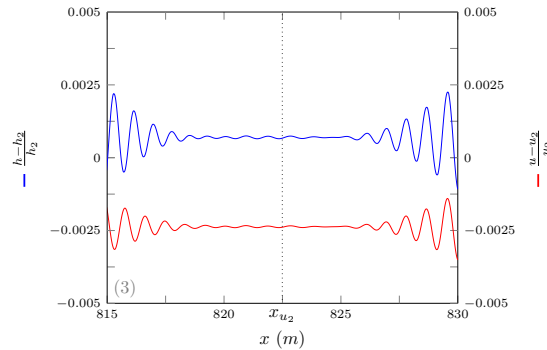


Figure 16: The relative difference between h and u and their comparisons h_2 and u_2 plotted around x_{u_2} for \mathcal{V}_3 's solutions with $\Delta x = 10/2^9 m$ for the smoothed dam-break problem with $\alpha = 0.1m$ at $t = 300s$.

and parameters at $t = 30s$ in Figure 11 has decayed away by $t = 300s$ in Figure 16. This is a trend throughout our numerical solutions where oscillation amplitude decreases over time around x_{u_2} , changing the structure of the solution. This can be seen by obtaining full convergence of the numerical solutions to the smoothed dam-break problem at $t = 3s$. The converged to numerical solutions for \mathcal{V}_3 are shown in Figure 18. From this figure it can be seen that the oscillation amplitudes for the numerical solutions for the smoothed dam-break problems with $\alpha = 0.4m$ and $\alpha = 0.1m$ are much larger at $t = 3s$ than they are at $t = 30s$ in Figure 4. Since we have demonstrated that our numerical solutions are good approximations to the true solution of the Serre equations at $t = 30s$ and $t = 3s$, decreasing oscillation amplitude around x_{u_2} over time must be a property of the Serre equations.

5.2.1. Contact discontinuity

El et al. [7] noted the presence of a ‘degenerate contact discontinuity’ which is the node in the \mathcal{S}_3 structure and travels at the mean fluid velocity in the bore.

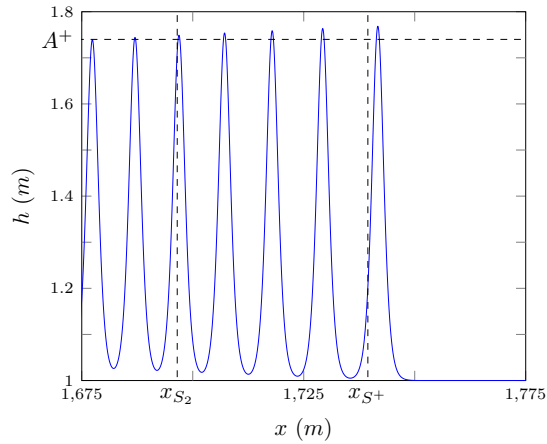


Figure 17: Numerical solution of \mathcal{V}_3 with $\Delta x = 10/2^9 m$ for the smoothed dam-break problem with $\alpha = 0.1m$ at $t = 300s$ around the front of the undular bore.

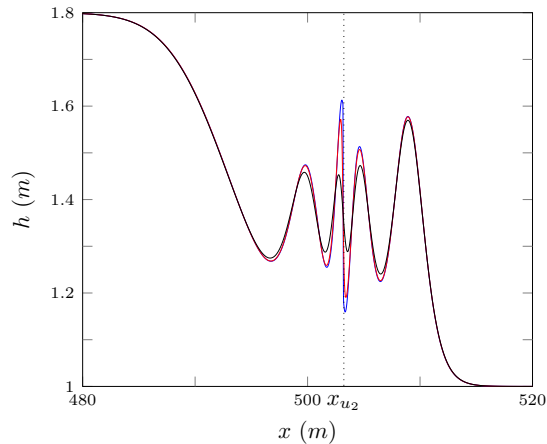


Figure 18: Numerical solution of \mathcal{V}_3 with $\Delta x = 10/2^{13} m$ for the smoothed dam-break problem with $\alpha = 0.001m$ (blue), $0.1m$ (red) and 0.4 (black) at $t = 3s$.

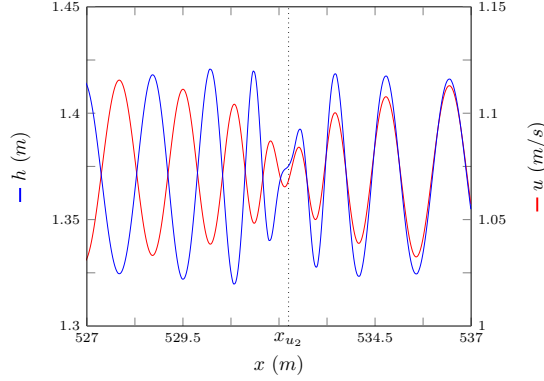


Figure 19: Numerical solution of \mathcal{V}_3 's with $\Delta x = 10/2^9 m$ for the smoothed dam-break problem with $\alpha = 0.1m$ at $t = 30s$ around the contact discontinuity.

We observe that as our numerical solutions evolve over time oscillations appear to be released from the contact discontinuity and travel away from it in both directions, leading to decay of amplitudes around the contact discontinuity. Therefore, the contact discontinuity is an important feature and its behaviour determines the structure of the oscillations in the middle of the undular bore.

The different speeds of the oscillations are determined by the phase velocity, which for the Serre equations linearised around the mean height \bar{h} and mean velocity \bar{u} in regions III and IV is

$$v_p = \bar{u} \pm \sqrt{g\bar{h}} \sqrt{\frac{3}{\bar{h}^2 k^2 + 3}} \quad (10)$$

with wave number k , it can be seen that as $k \rightarrow \infty$ then $v_p \rightarrow \bar{u}$ and as $k \rightarrow 0$ then $v_p \rightarrow \bar{u} \pm \sqrt{g\bar{h}}$. Since the contact discontinuity travels at the mean velocity inside the bore, it corresponds to very high wave number oscillations. The oscillations on the left travel slower than the contact discontinuity and are therefore lower wave number oscillations associated with the phase velocity $\bar{u} - \sqrt{g\bar{h}} \sqrt{3/(\bar{h}^2 k^2 + 3)}$. The oscillations on the right travel quicker than the contact discontinuity and are therefore lower wave number oscillations associated with the phase velocity $\bar{u} + \sqrt{g\bar{h}} \sqrt{3/(\bar{h}^2 k^2 + 3)}$.

These different phase velocities have two different behaviours for h and u . When the phase velocity is $\bar{u} + \sqrt{g\bar{h}} \sqrt{3/(\bar{h}^2 k^2 + 3)}$ we have oscillations where h and u are in-phase, while when the phase velocity is $\bar{u} - \sqrt{g\bar{h}} \sqrt{3/(\bar{h}^2 k^2 + 3)}$ we have oscillations where h and u are out-of-phase. This can be seen in Figure 19 for the numerical solutions of \mathcal{V}_3 with $\Delta x = 10/2^9 m$ for the smoothed dam-break problem with $\alpha = 0.1m$ at $t = 30s$.

5.3. Whitham Modulation Comparsion

El et al. [7] demonstrated that their Whitham modulation results approximated the numerical solutions of the smoothed dam-break problem well for a range of aspect

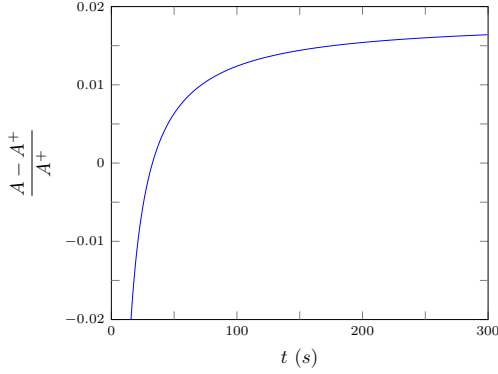


Figure 20: Relative difference between Whitham modulation result A^+ and the leading wave amplitude A from our numerical solutions of \mathcal{V}_3 with $\Delta x = 10/2^9 m$ for the smoothed dam-break problem with $\alpha = 0.1m$ over time.

492 ratios. However, we observe that the Whitham modulation results are an underestimate
493 compared to our numerical solutions.

494 This can be seen in Figure 20 as the relative difference between A^+ from El et al. [7]
495 and the leading wave amplitude of our numerical solution A does not converge to 0 over
496 time. Since we find that the numerical solutions for the smoothed dam-break problem
497 with $\alpha = 0.1m$ have converged for the front of the undular bore by $\Delta x = 10/2^8 m$ as
498 in Figure 11, our numerical solutions for A are considered reliable. We also note that
499 unlike the oscillations around x_{u_2} the leading wave amplitude increases over time.

500 The Whitham modulation results for the location of the leading wave x_{S^+} is a better
501 approximation than that given by the shallow water wave equations x_{S_2} , as can be seen
502 in Figure 17.

503 6. Conclusions

504 Utilising two finite difference methods of second-order and three finite difference
505 finite volume methods of various orders to solve the nonlinear weakly dispersive Serre
506 equations an investigation into the smoothed dam-break problem with varying steep-
507 ness was performed. Four different structures of the numerical solutions were observed
508 and demonstrated to be valid, the general trend of these structures is that an increase
509 in steepness increases the size and number of oscillations in the solution. This study
510 explains the different structures exhibited by the numerical results in the literature for
511 the smoothed dam-break problem for the Serre equations and uncovers a new result.
512 These results demonstrate that other methods in the literature could replicate our results
513 if their simulations are extended. Furthermore, these results suggest that this new result
514 and its associated structure is to be expected for the solution of the Serre equation to
515 the dam-break problem at least for short enough time spans.

516 We find that the analytical solution of the shallow water wave equations for the
517 dam-break problem provides a reasonable approximation to the mean height and velocity
518 inside the bore formed by the smoothed dam-break problem for the Serre equations.
519 Finally, we observe that the Whitham modulations results for the leading wave of an

undular bore do not correspond with our validated numerical results, and are only an approximation. However, the Whitham modulation results do provide a more accurate approximation to the location of the front of an undular bore than the shallow water wave equations.

- [1] D. Mitsotakis, D. Dutykh, J. Carter, On the nonlinear dynamics of the traveling-wave solutions of the Serre system, *Wave Motion* 70 (1) (2017) 166–182.
- [2] O. Le Métayer, S. Gavrilyuk, S. Hank, A numerical scheme for the Green-Naghdi model, *Journal of Computational Physics* 229 (6) (2010) 2034–2045.
- [3] C. Zoppou, S. Roberts, J. Pitt, A Solution of the Conservation Law Form of the Serre Equations, *The ANZIAM Journal* 57 (4) (2017) 385–394.
- [4] C. Zoppou, J. Pitt, S. Roberts, Numerical Solution of the Fully Non-Linear Weakly Dispersive Serre Equations for Steep Gradient Flows, *Applied Mathematical Modelling* 48 (2017) 70–95.
- [5] P. Bonneton, E. Barthélémy, F. Chazel, R. Cienfuegos, D. Lannes, F. Marche, M. Tissier, Recent advances in Serre-Green Naghdi modelling for wave transformation, breaking and runup processes, *European Journal of Mechanics B/Fluids* 30 (6) (2011) 589–597.
- [6] P. Bonneton, F. Chazel, D. Lannes, F. Marche, M. Tissier, A splitting approach for the fully nonlinear and weakly dispersive Green-Naghdi model, *Journal of Computational Physics* 230 (4) (2011) 1479–1498.
- [7] G. El, R. H. J. Grimshaw, N. F. Smyth, Unsteady undular bores in fully nonlinear shallow-water theory, *Physics of Fluids* 18 (2) (2006) 027104.
- [8] D. Mitsotakis, B. Ilan, D. Dutykh, On the Galerkin/Finite-Element Method for the Serre Equations, *Journal of Scientific Computing* 61 (1) (2014) 166–195.
- [9] C. H. Su, C. S. Gardner, Korteweg-de Vries equation and generalisations. III. Derivation of the Korteweg-de Vries equation and Burgers equation, *Journal of Mathematical Physics* 10 (3) (1969) 536–539.
- [10] D. Lannes, P. Bonneton, Derivation of asymptotic two-dimensional time-dependent equations for surface water wave propagation, *Physics of Fluids* 21 (1) (2009) 16601–16610.
- [11] M. Li, P. Guyenne, F. Li, L. Xu, High order well-balanced CDG-FE methods for shallow water waves by a Green-Naghdi model, *Journal of Computational Physics* 257 (2014) 169–192.
- [12] Y. A. Li, Hamiltonian Structure and Linear Stability of Solitary Waves of the Green-Naghdi Equations, *Journal of Nonlinear Mathematical Physics* 9 (2002) 99–105.
- [13] A. E. Green, P. M. Naghdi, A derivation of equations for wave propagation in water of variable depth, *Journal of Fluid Mechanics* 78 (2) (1976) 237–246.

- 558 [14] C. Wu, G. Huang, Y. Zheng, Theoretical solution of dam-break shock wave, Journal
559 of Hydraulic Engineering 125 (11) (1999) 1210–1215.
- 560 [15] A. A. Harten, High resolution schemes for hyperbolic conservation laws, Journal
561 of Computational Physics 49 (3) (1983) 357–393.
- 562 [16] G. El, M. Hoefer, Dispersive shock waves and modulation theory, Physica D:
563 Nonlinear Phenomena 333 (2016) 11–65.

564 **Appendix A.**

565 The methods \mathcal{E} and \mathcal{D} use the centred second-order finite difference approximation
 566 to the momentum equation (1b), denoted as \mathcal{D}_u . For the mass equation (1a) \mathcal{E} uses the
 567 two step Lax-Wendroff method, denoted as \mathcal{E}_h while \mathcal{D} uses a centred second-order
 568 finite difference approximation, denoted as \mathcal{D}_h .

569 *Appendix A.1. \mathcal{D}_u for the Momentum Equation*

570 First (1b) is expanded to get

$$571 \quad h \frac{\partial u}{\partial t} - h^2 \frac{\partial^2 u}{\partial x \partial t} - \frac{h^3}{3} \frac{\partial^3 u}{\partial x^2 \partial t} = -X \quad (\text{A.1})$$

573 where X contains only spatial derivatives and is

$$574 \quad X = uh \frac{\partial u}{\partial x} + gh \frac{\partial h}{\partial x} + h^2 \frac{\partial u}{\partial x} \frac{\partial u}{\partial x} + \frac{h^3}{3} \frac{\partial u}{\partial x} \frac{\partial^2 u}{\partial x^2} - h^2 u \frac{\partial^2 u}{\partial x^2} - \frac{h^3}{3} u \frac{\partial^3 u}{\partial x^3}. \quad (\text{A.2})$$

576 All derivatives are approximated by second-order centred finite difference approximations
 577 on a uniform grid in space and time, which after rearranging into an update
 578 formula becomes

$$579 \quad h_i^n u_i^{n+1} - (h_i^n)^2 \left(\frac{u_{i+1}^{n+1} - u_{i-1}^{n+1}}{2\Delta x} \right) - \frac{(h_i^n)^3}{3} \left(\frac{u_{i+1}^{n+1} - 2u_i^{n+1} + u_{i-1}^{n+1}}{\Delta x^2} \right) = -Y_i^n \quad (\text{A.3})$$

581 where

$$582 \quad Y_i^n = 2\Delta t X_i^n - h_i^n u_i^{n-1} + (h_i^n)^2 \left(\frac{u_{i+1}^{n-1} - u_{i-1}^{n-1}}{2\Delta x} \right) + \frac{(h_i^n)^3}{3} \left(\frac{u_{i+1}^{n-1} - 2u_i^{n-1} + u_{i-1}^{n-1}}{\Delta x^2} \right)$$

584 and

$$585 \quad X_i^n = u_i^n h_i^n \frac{u_{i+1}^n - u_{i-1}^n}{2\Delta x} + gh_i^n \frac{h_{i+1}^n - h_{i-1}^n}{2\Delta x} + (h_i^n)^2 \left(\frac{u_{i+1}^n - u_{i-1}^n}{2\Delta x} \right)^2$$

$$586 \quad + \frac{(h_i^n)^3}{3} \frac{u_{i+1}^n - u_{i-1}^n}{2\Delta x} \frac{u_{i+1}^n - 2u_i^n + u_{i-1}^n}{\Delta x^2} - (h_i^n)^2 u_i^n \frac{u_{i+1}^n - 2u_i^n + u_{i-1}^n}{\Delta x^2}$$

$$587 \quad - \frac{(h_i^n)^3}{3} u_i^n \frac{u_{i+2}^n - 2u_{i+1}^n + 2u_{i-1}^n - u_{i-2}^n}{2\Delta x^3}.$$

590 Equation (A.3) can be rearranged into an explicit update scheme \mathcal{D}_u for u given its
 591 current and previous values, so that

$$592 \quad \begin{bmatrix} u_0^{n+1} \\ \vdots \\ u_m^{n+1} \end{bmatrix} = A^{-1} \begin{bmatrix} -Y_0^n \\ \vdots \\ -Y_m^n \end{bmatrix} =: \mathcal{D}_u(\mathbf{u}^n, \mathbf{h}^n, \mathbf{u}^{n-1}, \Delta x, \Delta t) \quad (\text{A.4})$$

594 where A is a tri-diagonal matrix.

595 *Appendix A.2. Numerical Methods for the Mass Equation*

596 The two step Lax-Wendroff update \mathcal{E}_h for h is

$$597 \quad h_{i+1/2}^{n+1/2} = \frac{1}{2} (h_{i+1}^n + h_i^n) - \frac{\Delta t}{2\Delta x} (u_{i+1}^n h_{i+1}^n - h_i^n u_i^n), \\ 598 \\ 599$$

$$600 \quad h_{i-1/2}^{n+1/2} = \frac{1}{2} (h_i^n + h_{i-1}^n) - \frac{\Delta t}{2\Delta x} (u_i^n h_i^n - h_{i-1}^n u_{i-1}^n) \\ 601$$

602 and

$$603 \quad h_i^{n+1} = h_i^n - \frac{\Delta t}{\Delta x} (u_{i+1/2}^{n+1/2} h_{i+1/2}^{n+1/2} - u_{i-1/2}^{n+1/2} h_{i-1/2}^{n+1/2}). \\ 604 \\ 605$$

605 The quantities $u_{i\pm 1/2}^{n+1/2}$ are calculated using u^{n+1} obtained by applying \mathcal{D}_u (A.4) to u^n
606 then linearly interpolating in space and time to give

$$607 \quad u_{i+1/2}^{n+1/2} = \frac{u_{i+1}^{n+1} + u_{i+1}^n + u_i^{n+1} + u_i^n}{4} \\ 608$$

609 and

$$610 \quad u_{i-1/2}^{n+1/2} = \frac{u_i^{n+1} + u_i^n + u_{i-1}^{n+1} + u_{i-1}^n}{4}. \\ 611$$

612 Thus we have the following update scheme \mathcal{E}_h for (1a)

$$613 \quad \mathbf{h}^{n+1} = \mathcal{E}_h(\mathbf{u}^n, \mathbf{h}^n, \mathbf{u}^{n+1}, \Delta x, \Delta t). \quad (\text{A.5}) \\ 614$$

615 The second order centered finite difference approximation to the conservation of
616 mass equation (1a) is

$$617 \quad h_i^{n+1} = h_i^{n-1} - \Delta t \left(u_i^n \frac{h_{i+1}^n - h_{i-1}^n}{\Delta x} + h_i^n \frac{u_{i+1}^n - u_{i-1}^n}{\Delta x} \right). \\ 618$$

619 Thus we have an update scheme \mathcal{D}_h for all i

$$620 \quad \mathbf{h}^{n+1} = \mathcal{D}_h(\mathbf{u}^n, \mathbf{h}^n, \mathbf{h}^{n-1}, \Delta x, \Delta t). \quad (\text{A.6}) \\ 621$$

622 *Appendix A.3. Complete Method*

623 The method \mathcal{E} is the combination of (A.5) for (1a) and (A.4) for (1b) in the follow-
624 ing way

$$625 \quad \begin{aligned} \mathbf{u}^{n+1} &= \mathcal{D}_u(\mathbf{u}^n, \mathbf{h}^n, \mathbf{u}^{n-1}, \Delta x, \Delta t) \\ 626 \quad \mathbf{h}^{n+1} &= \mathcal{E}_h(\mathbf{u}^n, \mathbf{h}^n, \mathbf{u}^{n+1}, \Delta x, \Delta t) \end{aligned} \Bigg\} \mathcal{E}(\mathbf{u}^n, \mathbf{h}^n, \mathbf{u}^{n-1}, \mathbf{h}^{n-1}, \Delta x, \Delta t). \quad (\text{A.7})$$

627 The method \mathcal{D} is the combination of (A.6) for (1a) and (A.4) for (1b) in the follow-
628 ing way

$$629 \quad \begin{aligned} \mathbf{h}^{n+1} &= \mathcal{D}_h(\mathbf{u}^n, \mathbf{h}^n, \mathbf{h}^{n-1}, \Delta x, \Delta t) \\ 630 \quad \mathbf{u}^{n+1} &= \mathcal{D}_u(\mathbf{u}^n, \mathbf{h}^n, \mathbf{u}^{n-1}, \Delta x, \Delta t) \end{aligned} \Bigg\} \mathcal{D}(\mathbf{u}^n, \mathbf{h}^n, \mathbf{u}^{n-1}, \mathbf{h}^{n-1}, \Delta x, \Delta t). \quad (\text{A.8})$$